OPEN ACCESS



"Halfway to Rayleigh" and Other Insights into the Rossby Wave Instability

Eonho Chang ^{1,2} and Andrew N. Youdin ^{2,3} Tender of Craduate Interdisciplinary Program in Applied Mathematics, University of Arizona, Tucson, AZ 85721, USA ² Department of Astronomy and Steward Observatory, University of Arizona, Tucson, AZ 85721, USA ³ Lunar and Planetary Laboratory, University of Arizona, Tucson, AZ 85721, USA Received 2024 July 15; revised 2024 September 20; accepted 2024 September 29; published 2024 November 14

Abstract

The Rossby wave instability (RWI) is the fundamental nonaxisymmetric radial shear instability in disks. The RWI can facilitate disk accretion, set the shape of planetary gaps, and produce large vortices. It arises from density and/or temperature features, such as radial gaps, bumps, or steps. A general, sufficient condition to trigger the RWI is lacking, which we address by studying the linear RWI in a suite of simplified models, including incompressible and compressible shearing sheets and global, cylindrical disks. We focus on enthalpy amplitude and width as the fundamental properties of disk features with various shapes. We find analytic results for the RWI boundary and growth rates across a wide parameter space, in some cases with exact derivations and in others as a description of numerical results. Features wider than a scale height generally become unstable about halfway to Rayleigh instability, i.e., when the squared epicyclic frequency is about half the Keplerian value, reinforcing our previous finding. RWI growth rates approximately scale as enthalpy amplitude to the 1/3 power, with a weak dependence on width, across much of the parameter space. Global disk curvature affects wide planetary gaps, making the outer gap edge more susceptible to the RWI. Our simplified models are barotropic and height integrated, but the main results should carry over to more complex and realistic scenarios.

Unified Astronomy Thesaurus concepts: Hydrodynamics (1963); Astrophysical fluid dynamics (101); Planet formation (1241); Protoplanetary disks (1300)

1. Introduction

The Rossby wave instability (RWI) arises when radial disk structures, such as bumps or gaps, induce strong pressure gradients and non-Keplerian radial shear (R. V. E. Lovelace et al. 1999; H. Li et al. 2000). The RWI can generate large vortices (H. Li et al. 2001), for instance at the edges of planetary gaps (M. de Val-Borro et al. 2007), which affects planet migration (M.-K. Lin & J. C. B. Papaloizou 2010). The RWI also helps transport matter falling onto accretion disks (A. Kuznetsova et al. 2022).

Dust is trapped in both RWI-produced vortices and the rings that trigger the RWI, in agreement with the disk structures observed by the Atacama Large Millimeter/submillimeter Array (P. Pinilla & A. Youdin 2017). The RWI thus constrains observable rings and vortices (E. Chang et al. 2023), for instance, by regulating planet-carved gaps (N. P. Cimerman & R. R. Rafikov 2023). Dust trapped in such rings and vortices can trigger planet formation (E. Chiang & A. N. Youdin 2010; J. Drążkowska & C. P. Dullemond 2018; X. Hu et al. 2018; W. Lyra et al. 2024).

These significant consequences arise from simple considerations. The RWI does not require vertical motions, baroclinicity, or cooling, in contrast to the vertical shear instability (R. P. Nelson et al. 2013; M.-K. Lin & A. N. Youdin 2015) and other thermal disk instabilities (H. Klahr et al. 2023; G. Lesur et al. 2023). The RWI can be triggered by zonal flows arising from these hydrodynamic (N. Manger et al. 2020), or magnetohydrodynamic (MHD; A. Johansen et al. 2009) instabilities. RWI analyses that include 3D motions (H. Meheut

Original content from this work may be used under the terms of the Creative Commons Attribution 4.0 licence. Any further distribution of this work must maintain attribution to the author(s) and the title of the work, journal citation and DOI.

et al. 2012; M.-K. Lin 2013), cooling (S. Huang & C. Yu 2022), dust feedback (H. Liu & X.-N. Bai 2023), and nonideal MHD (C. Cui et al. 2024) are crucial for a complete understanding, and generally find modest corrections to idealized cases.

Even for simple cases, a general criterion for the onset of the RWI has been elusive. T. Ono et al. (2016) found that the RWI was triggered partway between the Lovelace and Rayleigh criteria for a variety of barotropic disk features. The Lovelace criterion, equivalent to a vortensity extrema in isentropic disks, is necessary but insufficient for the RWI (R. V. E. Lovelace et al. 1999). The Rayleigh criterion gives axisymmetric instability for disks with radially decreasing angular momentum somewhere, i.e., negative squared epicyclic frequency, κ^2 .

E. Chang et al. (2023) found that disk bumps (barotropic and baroclinic) triggered RWI when κ^2 was locally reduced to $\sim 60\%$ of the Keplerian value. We colloquially refer to this criterion as "halfway-to-Rayleigh" instability.

This work aims to develop a more fundamental understanding of the RWI boundary and growth rates, including the halfway-to-Rayleigh criterion. We develop scaling relations using the strength and width of disk features in enthalpy, the relevant thermodynamic quantity for radial shear. We start with simplified shearing-sheet models, which yield more analytic results and require fewer parameters, allowing for a more complete examination of parameter space. We then test against global disk models. This approach is motivated by previous shearing-sheet models studying incompressible (Y. Lithwick 2007) and compressible (R. Vanon & G. I. Ogilvie 2016) shear instability, linear Rossby modes (O. M. Umurhan et al. 2016), and nonlinear RWI with cooling (J. Fung & T. Ono 2021).

We present our method for studying the RWI with shearingsheet models in Section 2. Sections 3 and 4 present our results for the incompressible and compressible sheets, respectively. We compare to global disks in Section 5. A suggested starting point is the summary of our main results in Section 6.

2. Shearing-sheet RWI Models

2.1. The Compressible Shearing Sheet

The shearing sheet models a disk patch centered at radius R_c , rotating at the local Keplerian frequency, Ω , with Cartesian x-, y-, and z-coordinates oriented radially, azimuthally, and vertically. Vertical averaging gives the equations of motion (P. Goldreich & S. Tremaine 1978; B. M. Johnson & C. F. Gammie 2005)

$$\frac{D\Sigma}{Dt} = -\Sigma\nabla \cdot \mathbf{v},\tag{1a}$$

$$\left(\frac{D}{Dt} + 2\Omega\hat{z} \times\right) \mathbf{v} = 3\Omega^2 x \hat{x} - \frac{1}{\Sigma} \nabla P, \tag{1b}$$

$$D(P/\Sigma^{\gamma})/Dt = 0 \tag{1c}$$

for fluid velocity v, surface density Σ , and (height-averaged) pressure P, with $D/Dt = \partial/\partial t + v \cdot \nabla$. An ideal gas with adiabatic index γ , adiabatic motions, and no self-gravity or viscosity are assumed.

Combining Equations (1a) and (1b),

$$\frac{Dq}{Dt} = \frac{\nabla \Sigma \times \nabla P}{\Sigma^3} \cdot \hat{z},\tag{2}$$

shows that vortensity, $q \equiv (2\Omega + \hat{z} \cdot \nabla \times v)/\Sigma$, is conserved in the absence of baroclinic effects.

We consider an axisymmetric equilibrium with linear perturbations (using 0, 1 subscripts, respectively) as $\Sigma = \Sigma_0(x) + \Sigma_1$, $P = P_0(x) + P_1$, $v = v_0(x)\hat{y} + u_1\hat{x} + v_1\hat{y}$. Perturbed quantities have a Fourier dependence, e.g., $u_1 = \tilde{u}_1(x) \exp[\iota(k_y y - \omega t)]$. We henceforth drop the tilde.

The equilibrium orbital motion is

$$v_0 = -\frac{3}{2}\Omega x + \Delta v_0 = -\frac{3}{2}\Omega x + \frac{1}{2\Omega}\frac{d\Pi_0}{dx},$$
 (3)

where Π_0 is the equilibrium enthalpy, and $\Pi = \int dP/\Sigma$ gives the non-Keplerian motion, Δv_0 . The equilibrium vortensity, $q_0 = \kappa^2/(2\Omega\Sigma_0)$, depends on the squared epicyclic frequency

$$\kappa^2 = 2\Omega \left(2\Omega + \frac{dv_0}{dx} \right) = \Omega^2 + \frac{d^2\Pi_0}{dx^2}.$$
 (4)

The linear equations of motion for the Fourier amplitudes (given the same symbols as perturbed quantities for simplicity) are

$$-\iota \Delta \omega \Sigma_1 = -\frac{d}{dx} (\Sigma_0 u_1) - \iota k_y \Sigma_0 v_1, \tag{5a}$$

$$-\iota\Delta\omega u_1 - 2\Omega v_1 = -\frac{1}{\Sigma_0} \frac{dP_1}{dx} + \frac{\Sigma_1}{\Sigma_0^2} \frac{dP_0}{dx},\tag{5b}$$

$$-\iota \Delta \omega v_1 + \frac{\kappa^2}{2\Omega} u_1 = -\iota k_y \frac{P_1}{\Sigma_0},\tag{5c}$$

$$-i\Delta\omega\left(\frac{P_1}{P_0} - \gamma\frac{\Sigma_1}{\Sigma_0}\right) = -u_1\frac{d\ln(P_0/\Sigma_0^{\gamma})}{dx},\tag{5d}$$

with Doppler-shifted frequency, $\Delta\omega \equiv \omega - v_0(x)k_y$. We define a squared sound speed $c_0^2 \equiv \gamma P_0/\Sigma_0$, scale height $H_0 \equiv c_0/\Omega$,

(inverse) entropy length scale of

$$L_{\rm S}^{-1} \equiv \frac{1}{\gamma} \frac{d \ln(P_0/\Sigma_0^{\gamma})}{dx} \tag{6}$$

and radial buoyancy frequency of

$$N^2 \equiv -\frac{1}{\gamma \Sigma_0} \frac{dP_0}{dx} \frac{d \ln(P_0/\Sigma_0^{\gamma})}{dx} = -\frac{c^2}{\gamma L_S} \frac{d \ln(P_0)}{dx}.$$
 (7)

Manipulations yield an ordinary differential equation (ODE) for $\Psi \equiv P_1/\Sigma_0$,

$$\Psi'' + B(x)\Psi' = C(x)\Psi, \tag{8}$$

the shearing-sheet version of Equation (15) in H. Li et al. (2000) with primes for the x-derivatives, $B \equiv d \ln \mathcal{F}/dx$, and

$$\mathcal{F} \equiv \frac{\Sigma_0 \Omega^2}{\kappa^2 + N^2 - \Delta \omega^2},\tag{9a}$$

$$C \equiv k_y^2 + \frac{\Sigma_0}{\mathcal{F}H_0^2} + \frac{2\Omega k_y B}{\Delta \omega} + C_2, \tag{9b}$$

$$C_2 \equiv \frac{1 - L_S'}{L_S^2} + \frac{B}{L_S} + \frac{4\Omega k_y}{\Delta \omega L_S} - \frac{k_y^2 N^2}{\Delta \omega^2}.$$
 (9c)

This work considers isentropic equilibria with $C_2 = 1/L_S = N^2 = 0$.

The corotation resonance at $\Delta\omega = 0$ defines a corotation radius, x_c , where $\Re[\Delta\omega(x_c)] = 0$. At the Lindblad resonances, where $\Delta\omega^2 = \kappa^2 + N^2$ and $1/\mathcal{F} = 0$, B is singular.

The Schrödinger form of Equation (8) uses $\Xi = \sqrt{\mathcal{F}}\Psi$ to obtain (T. Ono et al. 2016)

$$\Xi'' = D(x)\Xi,\tag{10a}$$

$$D = \frac{B'}{2} + \frac{B^2}{4} + C. \tag{10b}$$

We solve Equation (8) since Ξ is singular at Lindblad resonances, but D is a useful effective potential.

2.2. The Incompressible Shearing Sheet

For the incompressible shearing sheet (ISS; H. N. Latter & J. Papaloizou 2017), we take the limit $\gamma \to \infty$, so that Equations (1a) and (1c) give $\nabla \cdot \mathbf{v} = 0$. We replace $\nabla P/\Sigma = \nabla \Pi$ in Equation (1b). The equilibrium is set by the choice of $\Pi_0(x)$, from which $v_0(x)$ and κ^2 follow Equations (3) and (4). The perturbed flow obeys a stream function, ψ , as $u_1 = -\iota k_y \psi$, $v_1 = \psi'$.

The vorticity $\zeta=(\nabla\times \mathbf{v})\cdot\hat{z}$, with equilibrium $\zeta_0=v_0'(x)$ and perturbation $\zeta_1=\psi''-k_y^2\psi$ is conserved $D\zeta/Dt=0$. Thus,

$$-\iota \Delta \omega \zeta_1 = -\zeta_0' u_1, \tag{11}$$

which gives

$$\psi'' = \left(k_y^2 + \frac{{v_0}''}{v_0 - \omega/k_y}\right)\psi \equiv D_{\rm inc}(x)\psi,\tag{12}$$

the famous Rayleigh equation for nonrotating incompressible shear flows. Coriolis forces set v_0 , but rotation is otherwise absent (see Y. Lithwick 2007).

There is vast literature on this equation (P. G. Drazin & W. H. Reid 2004). Relevant results include Rayleigh's theorem

that a vorticity extrema, $\zeta_0'(x) = 0$, is required for instability. Fjørtoft's theorem further states that this inflection point must be a maximum in $|\zeta_0(x)|$. Since disks have $\zeta_0(x) < 0$, instability requires a (signed) vorticity minimum.

Fjørtoft's theorem agrees with the interpretation of $D_{\rm inc}$ as a potential since for corotation at a vorticity minimum $\Re(D_{\rm inc}) < 0$ near corotation for long wavelengths, $k_y \to 0$. We further see that long wavelengths are the most unstable. When applied to compressible, barotropic disks, a *vortensity* minimum is required for instability.

Compared to the compressible case, we might expect $D \to D_{\rm inc}$ in an incompressible limit, so we make a technical clarification that this limiting behavior does not occur. Despite a shared k_y^2 term, we find that the corotation terms differ by a factor of 4 in a relevant limit. Specifically, we place the Lindblad resonances far from corotation with the $k_y W \ll 1$ limit (for the feature width, W, defined more precisely in Equations (13) and (14). Then the incompressible limit (with constant Σ_0) has $\mathcal{F} \propto 1/\kappa^2$ and $2\Omega B/\Delta\omega \to -4v_0''/\Delta\omega$. Thus, the compressible corotation term is 4 times larger than the corresponding term in $D_{\rm inc}$. This surprising result is possible since D has additional relevant terms and is a potential for a different fluid quantity. Despite this difference, our compressible results have a well-behaved incompressible limit (Section 4).

2.3. Disk Features

To understand the universal features of RWI, we consider various disk structures, including bumps, gaps, and steps. Our compressible and incompressible models share a common equilibrium enthalpy $\Pi_0(x)$ and thus $\nu_0(x)$. Our parameterization

$$\Pi_0(x) = \Pi_b + \Delta \Pi S(x/W) \tag{13}$$

has two constants, the reference value Π_b (which only affects compressible models) and amplitude $\Delta\Pi>0$. This work considers the shapes

$$S(X) = \begin{cases} G(X) & \text{bump} \\ 1 - G(X) & \text{gap} \\ \frac{1 - \tanh(X)}{2} & \text{drop} \\ \frac{1 + \tanh(X)}{2} & \text{jump} \end{cases}$$
(14)

for $G(X) = \exp(-X^2/2)$. The scaled distance $X \equiv x/W$ depends on the width parameter, W. With this definition, all S values vary from 0 to 1 over a length scale of order W. Since $\Pi_b = \min(\Pi_0(x)) > 0$, all $\Pi_0(x) > 0$.

We describe some properties of our shape functions next, then apply them to compressible models in Section 2.3.2.

2.3.1. Shape Functions

Figure 1 plots (in the top row) our enthalpy features. The scaled amplitude

$$\mathcal{J} \equiv \Delta \Pi / (\Omega W)^2 \tag{15}$$

measures a feature's vorticity amplitude.

The middle row of Figure 1 plots κ^2 . The location of vorticity (and κ^2) minima is $x_{\rm m} = 0$ for bumps, $\pm \sqrt{3} W$ for gaps—which have a pair of vorticity minima—and

 $W \ln(2 \pm \sqrt{3})/2 \simeq \pm 1.32W$, for jumps and drops, respectively. The location of vortensity minima, relevant for compressible flows, will be slightly shifted.

The inner and outer gap edges are symmetrically equivalent in the shearing sheet. So are the drop and jump cases. Henceforth, the "step" case refers to both.

Rayleigh instability occurs for $\min(\kappa^2) < 0$ and requires vertical motions to be absent from our model. The Rayleigh instability is still highly relevant and occurs for $\mathcal{J} > \mathcal{J}_{\kappa} \gtrsim 1$. Specifically, from Equations (4) and (13)

$$\frac{\kappa^2}{\Omega^2} = 1 + \mathcal{J}\frac{d^2S}{dX^2} \tag{16}$$

and $\mathcal{J}_{\kappa} \equiv 1/\text{max}(-d^2S/dX^2) = 1$ for bumps, 2.241 for gaps, and 2.598 for steps. Thus, $\min(\kappa^2) = (1 - \mathcal{J}/\mathcal{J}_{\kappa})\Omega^2$ in the shearing sheet. For global models, κ^2 also depends on W/R_c (Section 5.2). This dependence vanishes in the shearing-sheet limit, $W/R_c \ll 1$.

The bottom row of Figure 1 plots the incompressible effective potential as $D_{\rm inc} - k_y^2$ (Equation (12)). The corotation radius is at a vorticity minimum, $x_{\rm m}$, with phase speed $c_\omega = \omega/k_y = v_0(x_{\rm m})$. This choice removes the corotation singularity and gives (consistent with Fjørtoft's theorem) a negative potential well for trapped modes. The compressible potential D behaves similarly, but waves also propagate exterior to Lindblad resonances, where D < 0 (see Figure 2).

2.3.2. Compressible Shearing-sheet Features

The compressible shearing-sheet (CSS) model requires not just $\Pi_0'(x)$ but also Σ_0 and P_0 . We consider polytropic models with $P_0/P_b = (\Sigma_0/\Sigma_b)^\Gamma$, with reference values Σ_b , P_b . The structure index Γ could differ from the adiabatic index γ (but does not here, see below).

The polytropic enthalpy

$$\Pi_0 = \int \frac{dP_0}{\Sigma_0} = \frac{\Gamma}{\Gamma - 1} \frac{P_0}{\Sigma_0} \tag{17}$$

matches Equation (13) for

$$\Sigma_0 = \Sigma_b \left[1 + \frac{\Delta \Pi}{\Pi_b} S(x/W) \right]^{\frac{1}{\Gamma - 1}}, \tag{18}$$

and $\Pi_b = \Gamma P_b / [(\Gamma - 1)\Sigma_b]$.

This compressible polytropic model requires three additional parameters, besides $k_y W$ and \mathcal{J} : γ , Γ and $H \equiv c/\Omega$ with

$$c^2 \equiv \gamma P_b / \Sigma_b = \gamma (\Gamma - 1) \Pi_b / \Gamma. \tag{19}$$

We drop the b subscripts from the reference H and c values for convenience. We do not need $\Sigma_{\rm b}$ or $P_{\rm b}$ independently, as Equation (8) only depends on logarithmic derivatives of Σ_0 and P_0 .

To reduce parameter space, we fix $\Gamma = \gamma = 4/3$ for an adiabatic sheet with $N^2 = 1/L_S = 0$. A diatomic gas with $\gamma_{\rm 3D} = 7/5$ corresponds to our height integrated $\gamma = (3\gamma_{\rm 3D} - 1)/(\gamma_{\rm 3D} + 1) = 4/3$ (P. Goldreich et al. 1986; H. Li et al. 2000). Thus, H is the only additional free parameter our compressible models.

The limits $\Gamma \to 1$, ∞ describe constant temperature and Σ_0 features, respectively (E. Chang et al. 2023). For completeness,

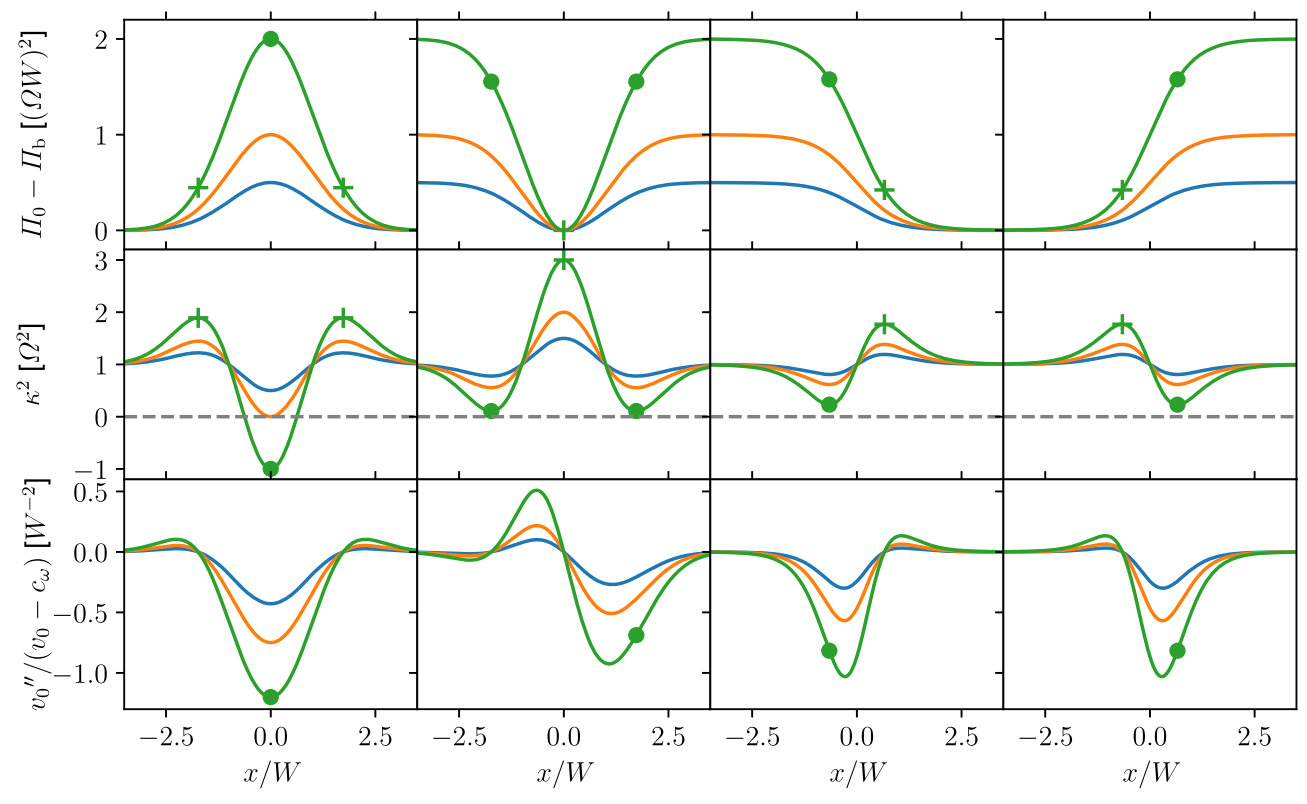


Figure 1. Radial profiles of shearing-sheet equilibria for (from left to right) bumps, gaps, drops, and jumps of width W and amplitude $\mathcal{J} = \Delta \Pi/(\Omega W)^2 = 0.5, 1, 2$ (blue, orange, and green curves). Top row: enthalpy. Middle row: epicyclic frequency squared, κ^2 . Minima (dots) and maxima (pluses) of vorticity (and equivalently κ^2) are marked in all rows. Bottom row: the effective potential D_{inc} for marginally stable RWI (offset by k_y^2 , see the text).

the $\Gamma \rightarrow 1$ limit of Equation (18) is

$$\Sigma_0 = \gamma \frac{P_0}{c^2} = \Sigma_b \exp\left[\frac{\gamma \Delta \Pi}{c^2} S\left(\frac{x}{W}\right)\right],\tag{20}$$

with $\Pi_b(\Gamma - 1) \rightarrow c^2/\gamma$ remaining finite.

2.4. Boundary Conditions and Solution Methods

Solving our second-order ODEs requires a pair of boundary conditions, applied at large distances $|x| \gg W$, $1/k_y$, and (for the compressible case) $|x| \gg H$.

For the incompressible case (Equation (12)), $D_{\text{inc}} \rightarrow k_y^2$ at large |x|. Physical solutions decay exponentially, with boundary conditions,

$$\psi' = \pm k_{\nu}\psi,\tag{21}$$

at large $\mp |x|$.

For the compressible case, boundary conditions exterior to the Lindblad resonances should match outgoing density waves. We seek WKB solutions of the form $\Psi \sim A(x) \exp(i \int_{-\infty}^{x} k_x(\chi) d\chi)$. Compared to previous works (H. Li et al. 2000; T. Ono et al. 2016; E. Chang et al. 2023) that used just k_x , we find A(x) to lowest order, which improves some numerical results.

First, we confirm that outgoing waves have $k_x(x) > 0$. The large |x|, Keplerian limit gives $\Delta\omega \to 3\Omega k_y x/2$, $\mathcal{F}/\Sigma_0 \to -\Omega^2/\Delta\omega^2$, $B \to -3\Omega k_y/\Delta\omega \to -2/x$, and $C \simeq D \to -(\Delta\omega/c_0)^2 \to [3k_y x/(2H_0)]^2$. To the lowest WKB order, Equation (8) gives $k_x = \pm \sqrt{-C}$, i.e., $\Delta\omega^2 = (k_x c_0)^2$. The group velocity

$$\frac{\partial \omega}{\partial k_x} = \frac{\partial \Delta \omega}{\partial k_x} \approx \frac{k_x c^2}{\Delta \omega} \approx \frac{2k_x H_0}{3k_x x} c \tag{22}$$

confirms that $k_x > 0$ for outgoing waves (as $k_y > 0$ by convention).

For more accuracy, we adopt the physical optics solution to Equation (10a) as

$$\Xi \sim \frac{c_{\Xi}}{\sqrt{k_{x,D}}} \exp\left(i \int_{-\infty}^{x} k_{x,D}(\chi) d\chi\right),$$
 (23)

with $k_{x,D} = \sqrt{-D}$ (the desired positive root) and c_{Ξ} an arbitrary (complex) constant.

Taking the derivative gives the boundary condition

$$\Xi' = \left(i\sqrt{-D} - \frac{1}{4D}\frac{dD}{dx}\right)\Xi. \tag{24}$$

The desired boundary condition for $\Psi = \Xi/\sqrt{\mathcal{F}}$ follows as

$$\Psi' = \left(i\sqrt{-D} - \frac{B}{2} - \frac{1}{4D}\frac{dD}{dx}\right)\Psi. \tag{25}$$

At large |x|, $d \ln(D)/dx/4 \rightarrow 1/(2x)$, so that $|\Xi| \propto 1/|x|^{1/2}$ and $|\Psi| \propto |x|^{1/2}$, in agreement with our numerical solutions.

Our numerical solutions use the shooting method. At the inner boundary, x_i , we pick an arbitrary $\psi(x_i)$ or $\Psi(x_i)$ and set the derivative with the boundary condition, Equation (21) or Equation (25). We integrate with the Dormand-Prince method ("DOP853") implemented in scipy.integrate.solve_ivp. The integrated solution deviates from the outer boundary condition. Using Muller's method, we minimize the residual error and find the complex eigenvalue $\omega \equiv \omega_r + \iota s$. The shooting method requires good initial guesses. We use known solutions to gradually explore parameter space.

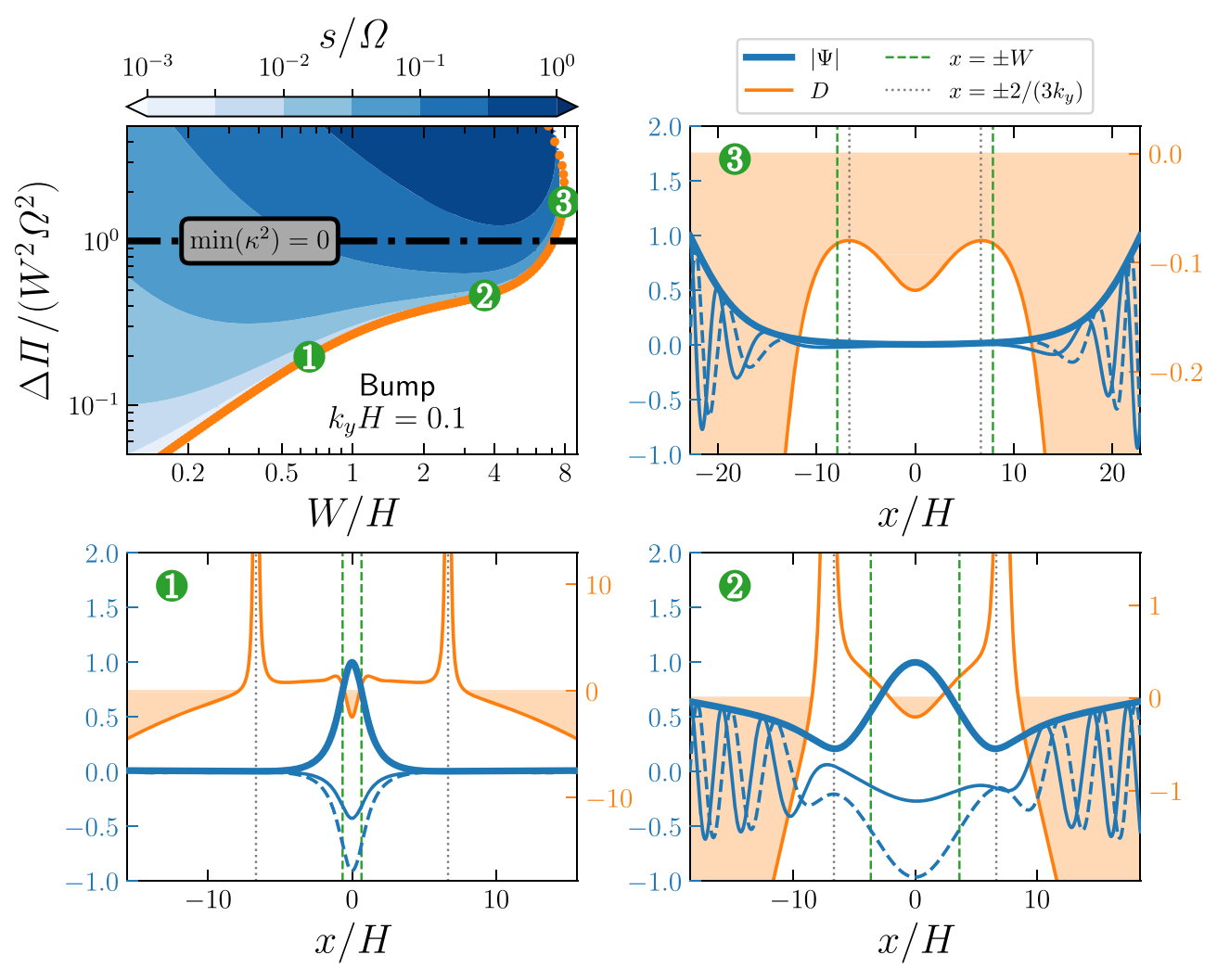


Figure 2. Top left: along the RWI boundary for $k_yH=0.1$ in a CSS bump, numbers \odot — \odot mark the modes investigated. Other panels: the effective potential D (orange curves, with negative regions shaded) and pressure perturbation Ψ (blue curves for magnitude [thick], real and imaginary parts [thin solid and dashed]) of the numbered modes, with the bump width (green dotted lines) and nominal (Keplerian) location of Lindblad resonances (gray dotted lines) marked. \odot : distant Lindblad resonances, with a trapped mode in the Rossby zone. \odot : the trapped Rossby mode couples to density waves exterior to nearby Lindblad resonances. \odot : no Lindblad resonances since $\kappa^2 < 0$, and a "leaky" potential (negative everywhere). This Rayleigh unstable region is not our focus.

For global models, we apply the same method but solve Equation (15) in H. Li et al. (2000) instead of Equation (8).

We have validated our numerical result in several ways, including adjusting the outer boundary positions, finding the incompressible limit of compressible results, and using different methods for the RWI stability boundary (below). Similar to H. Li et al. (2000), we derive an energy equation from Equation (5a), which after azimuthal averaging (denoted by brackets) is

$$\frac{\partial}{\partial t} \left[\frac{\Sigma_0}{2} \left(\langle |\mathbf{v}_1|^2 \rangle + \frac{\langle \Psi^2 \rangle}{c^2} \right) \right]
= -\frac{d\mathbf{v}_0}{dx} \Sigma_0 \langle \mathbf{u}_1 \mathbf{v}_1 \rangle - \frac{d}{dx} \langle P_1 \mathbf{u}_1 \rangle.$$
(26)

We verified that growth rates and eigenfunctions found by our numerical method satisfy this relation, over a range of parameters, \mathcal{J} , W/H, and $k_{\nu}H$.

2.4.1. Locating the Stability Boundary

We find marginally stable modes using a simplified method (T. Ono et al. 2016). With s = 0, we fix the corotation radius,

 x_c , to vorticity (or vortensity) minima for incompressible (or compressible) models, which sets $\omega = k_y v_0(x_c)$. With this choice, the ODE has real coefficients, and no corotation singularity, as shown in Figure 1 for the incompressible case.

One physical parameter, usually k_yW or W/H, varies as the shooting parameter (and eigenvalue). With other parameters held fixed, this method finds marginally stable solutions. For the incompressible model, this method uses $\psi(x)$ purely real. For the compressible models, $\Psi(x)$ has a complex boundary condition (Equations (24), (25)). Thus, the eigenvalue (W/H) can acquire an imaginary part, which is unphysical. Usually, this imaginary part is negligibly small ($\lesssim 10^{-3}$ of the real part), which validates the method. Figure 2 shows examples of solutions obtained with this method. Growth rates away from the stability boundary are also mapped using the usual method.

For more extreme parameters—near Rayleigh instability and for $k_y W \simeq 1$ (placing Lindblad resonances in the Rossby zone)—this method can fail, as it does (for different reasons) in baroclinic disks (E. Chang et al. 2023). In these cases, we simply measure where s drops to small values.

It is numerically difficult to find growth rates with $s/\Omega \lesssim 10^{-3}$. Since both methods agree on the stability

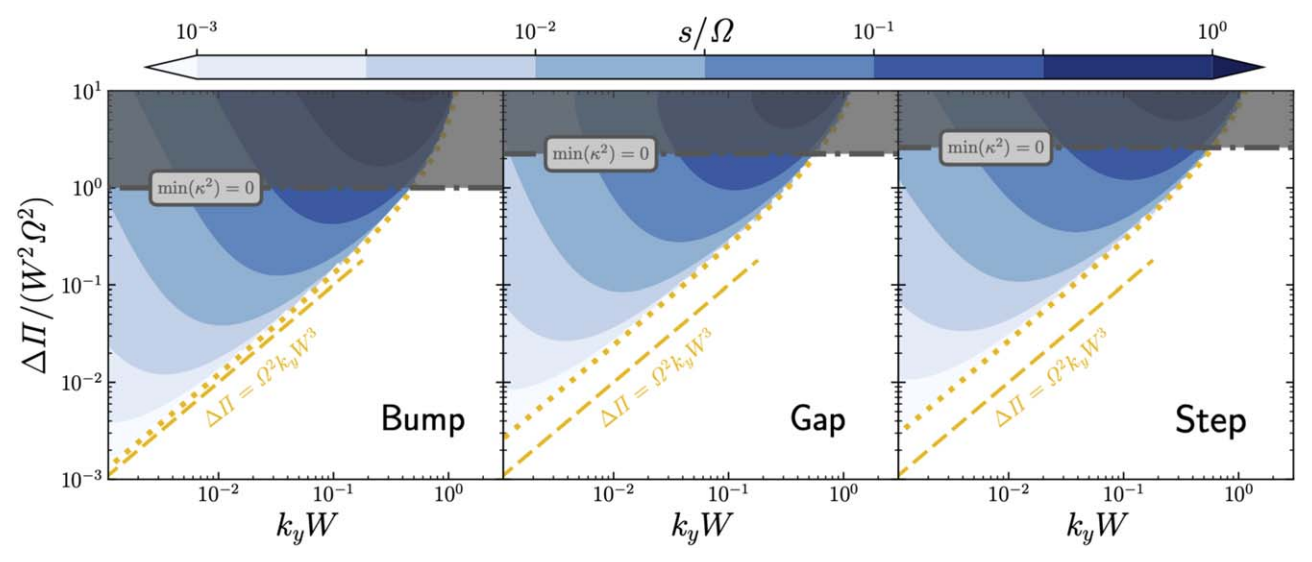


Figure 3. Incompressible RWI growth rate s for (left to right) bump, gap, and step features against scaled enthalpy amplitude $\mathcal{J} \equiv \Delta \Pi/(W^2\Omega^2)$ and the ratio of feature width to azimuthal wavelength, k_yW . The RWI boundary (dotted yellow), $\mathcal{J} = k_yW$ reference line (dashed yellow), and Rayleigh unstable regions (gray shaded) are shown.

boundary location (when this simplified method works), the stability boundary is relatively sharp.

3. Incompressible Results

Figure 3 maps RWI growth rates for various shapes in the ISS. For a given shape, the incompressible RWI is completely described by the parameters for amplitude, $\mathcal{J} = \Delta \Pi/(\Omega W)^2$, and width (scaled to wavenumber), k_yW . We describe the incompressible stability boundary, growth rates, and eigenfunctions below.

3.1. Incompressible Stability Boundary

The dotted yellow curves in Figure 3 show the stability boundary, found as described in Section 2.4.1. RWI occurs for larger \mathcal{J} or smaller k_yW than this boundary. No modes (stable, unstable, or damped) exist on the other side.

The stability boundary is best understood as smoothly connected $\mathcal{J} \ll 1$ and $J \gg 1$ limits. For $\mathcal{J} \ll 1$, the stability boundary follows $\mathcal{J} \simeq f_{\text{MS}} k_{\nu} W$, or

$$\Delta\Pi = f_{\rm MS} \Omega^2 k_{\rm v} W^3, \tag{27}$$

with $f_{\rm MS} \simeq 1.20, 2.39, 2.65$ for the bumps, gaps, and steps, respectively.

For $\mathcal{J} \gg 1$, the stability boundary is simply $k_y W = g_{MS}$, with $g_{MS} = \sqrt{2}$, 1.05, 2.0 for the bump, gap, and step cases, respectively. While large \mathcal{J} values are Rayleigh unstable, this limiting behavior explains why the stability curve steepens for $\mathcal{J} \gtrsim 1$.

These limiting behaviors can be understood in several ways, as described below.

3.1.1. Intuitive Explanations

The $\mathcal{J} \gg 1$ instability condition, $k_y W < g_{\rm MS}$, follows the idea that counterpropagating Rossby waves (CRWs) drive shear instability (E. Heifetz et al. 1999). For simplicity, we consider bumps and examine the approximate condition for CRWs at $x \simeq \pm W$ to maintain a stationary phase, with phase speed $c_\omega = \omega/k_v = 0$, as illustrated in Section 3.3.

With a $\psi(x) \propto \exp(ik_x x)$ WKB approximation, Equation (12) gives $c_{\omega} = v_0 + v_0''/(k_x^2 + k_y^2)$. At $x = \pm W$, $v_0/(\Omega W) \sim \mp (1 + \mathcal{J})$ roughly accounts for Keplerian and non-Keplerian flows, and $v_0'' \sim \pm \mathcal{J}\Omega/W$. Taking $k_x W \simeq 1$ matches the local wave packet to feature size, giving

$$\frac{v_0''}{k_x^2 + k_y^2} \sim \pm \frac{\mathcal{J}}{1 + (k_y W)^2} (\Omega W). \tag{28}$$

Thus, $c_{\omega} = 0$ requires $\mathcal{J} \sim (1 + \mathcal{J})(1 + (k_y W)^2)$.

For $\mathcal{J} \gg 1$, this rough analysis requires $1 \sim 1 + (k_y W)^2$ or $k_y W \lesssim 1$ for phase matching and instability, as desired. For $\mathcal{J} \ll 1$, this analysis fails.

Instead, for the $\mathcal{J} \ll 1$ boundary, another WKB analysis applies. Since $k_y W \ll 1$, waves have a shallow decay at large |x|/W, as $\psi \propto \exp(-k_y |x|)$. To match this decay, the slope across the Rossby zone must change sign, but only change magnitude by a small amount, $\Delta \Phi \equiv W \psi'|_{-W}^W/\psi \sim -k_y W$.

Across corotation, the slope change from WKB oscillations, $\psi \propto \exp(i\sqrt{-D_{\rm inc}}x)$, is

$$\Delta \Phi = W \int_{-W}^{W} \psi'' dx / \psi \sim D_{\rm inc} W^2 \sim -\mathcal{J}, \tag{29}$$

where the depth of the potential near corotation is $D_{\rm inc} \simeq -\mathcal{J}/W^2$ (Figure 1). A trapped mode thus requires $\mathcal{J} \sim k_y W$, in agreement with the stability boundary. The small change in wave phase, $\sqrt{-D_{\rm inc}}\,W \sim \sqrt{\mathcal{J}} \ll 1$, explains the failure of standard WKB theory for $\mathcal{J} \ll 1$, as noted above.

For a more physical explanation of the $\mathcal{J} \ll 1$ stability boundary, we briefly summarize the analysis of shearing waves by Y. Lithwick (2007). Shearing waves interact with axisymmetric disk features of width W and vorticity amplitude $\Delta \zeta_0 \simeq \Delta \Pi/(\Omega W^2)$.

A leading wave with initial radial wavenumber $k_x(t=0) \simeq -1/W$ and fixed $k_y > 0$ swings through a radial orientation, $k_x(t_{\rm sw}) = 0$, in time $t_{\rm sw} = (2k_x(0)/(3\Omega k_y) \simeq 1/(\Omega k_y W)$ since for $\mathcal{J} \ll 1$ the flow is nearly Keplerian (P. Goldreich & D. Lynden-Bell 1965). While swinging, the wave couples to the disk feature and spawns a new leading

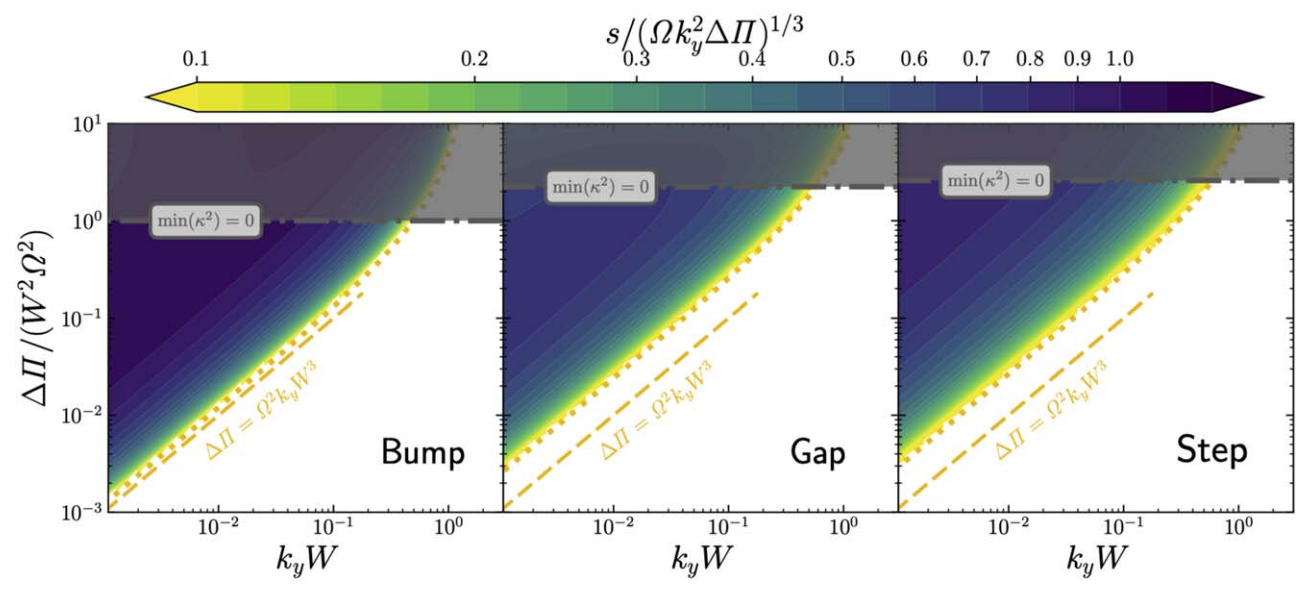


Figure 4. Same as Figure 3, except incompressible growth rates are scaled by a characteristic rate $(\Omega k_y^2 \Delta \Pi)^{1/3}$. Away from the stability boundary, these scaled rates vary only moderately.

wave. The amplitude of successive waves increases if $\Delta \zeta_0 t_{\rm sw} \gtrsim 1$ or $\Delta \Pi \gtrsim \Omega^2 k_y W^3$, reproducing the $\mathcal{J} \ll 1$ instability criterion.

3.1.2. More Quantitative Explanations

The above arguments can be made more rigorous. For $\mathcal{J} \ll 1$, Y. Lithwick (2007) couples the physical argument ($\Delta \zeta t_{\rm sw} \gtrsim 1$) to a stability boundary given by the integral

$$k_{y}\Omega = \frac{1}{3} \int_{-\infty}^{\infty} \frac{d\zeta_{0}/dx}{x - x_{0}} dx,$$
 (30)

with the vorticity minimum at x_c . This result reproduces Equation (27), and for our shapes, precisely gives $f_{MS} = 6/I_{MS}$, with

$$I_{\rm MS} = \int_{-\infty}^{\infty} \frac{S'''(X)}{X - X_{\rm c}} dX,\tag{31}$$

where $X_{\rm c}=x_{\rm c}/W$. Integrating $I_{\rm MS}$ reproduces our numerical results. For bumps, $f_{\rm MS}=3/\sqrt{2\pi}$, and gaps, $f_{\rm MS}=6/\sqrt{2\pi}$. The numerically integrated $I_{\rm MS}$ for steps is also consistent.

For $\mathcal{J}\gg 1$, the stability boundary $k_yW=\sqrt{2}$ for the bump case can be derived exactly. The $\mathcal{J}\to\infty$ limit gives a parabolic potential well $D_{\rm inc}W^2\to (k_yW)^2+3-(x/W)^2$. This potential has quantized bound states of "energy" $E=3-(k_yW)^2=2n+1$ for $n=0,1,\ldots$ (e.g., M. O. Manasreh 2012, Appendix E). For $(k_yW)^2>0$, only the n=0 bound state exists, which demonstrates the lack of RWI modes with higher radial order. This bound state has $k_yW=\sqrt{2}$, as claimed.

For all shapes, a necessary condition for RWI follows from the requirement that $D_{\rm inc} < 0$. This necessary condition is only close to the stability boundary for $\mathcal{J} \gtrsim 1$. For $\mathcal{J} \gg 1$, this necessary condition is $k_y W < \sqrt{3}$ for gaps and bumps and $k_y W < 2$ for steps. These simple necessary conditions are close to, but less strict than, the sufficient conditions for instability.

3.2. Incompressible Growth Rates

Figure 3 shows that RWI growth rates increase with \mathcal{J} and with k_yW , except near marginal stability. While it is easier to trigger RWI for long wavelengths (small k_yW), growth rates well into the unstable region are faster for smaller wavelengths (large k_yW). The smooth variations in growth rates, especially away from the stability boundary, suggest an analytic scaling.

Figure 4 plots growth rates scaled by the characteristic rate

$$s_{\rm inc} \equiv (\Omega k_y^2 \Delta \Pi)^{1/3}. \tag{32}$$

This approximation is reasonably good, aside from the rapid decay near the stability boundary.

In the $k_y W \ll 1$ limit, Y. Lithwick (2007) derives the growth rate $s/\Omega = (3/2)\alpha k_y W$, where α follows from the complex integral constraint on α and β :

$$k_y \Omega = \frac{1}{3W} \int_{-\infty}^{\infty} \frac{d\zeta_0/dX}{(X-\beta)^2 + \alpha^2} (X-\beta + i\alpha) dX.$$
 (33)

This result reduces to Equation (30) for marginal stability, where $\beta \rightarrow X_c$. The analysis is simplest for bumps, where symmetry about the vorticity minimum gives $\beta = 0$, and the imaginary part of the integral vanishes.

Our parameterization, with $S_{\rm B}$ for the bump shape, gives

$$\frac{k_y W}{\mathcal{J}} = \frac{1}{f_{\text{US}}(\alpha)} \equiv \frac{1}{6} \int_{-\infty}^{\infty} \frac{X S_{\text{B}}^{"'}(X)}{X^2 + \alpha^2} dX. \tag{34}$$

The function $f_{\rm US}(\alpha)$ for unstable modes, gives $f_{\rm US}(0) = f_{\rm MS}$ at marginal stability. Equation (34) only gives simple expressions in limiting cases.

For $\alpha \ll 1$, $\pi \alpha/2 \rightarrow 1/f_{\rm MS} - k_y W/\mathcal{J}$ gives the rise in growth rates near the stability boundary as

$$\frac{s}{\Omega} \approx \frac{3}{\pi} k_y W \left(\frac{1}{f_{\rm MS}} - \frac{k_y W}{\mathcal{J}} \right).$$
 (35)

The $\alpha \to \infty$ limit gives $f_{\rm US} \to \alpha^4/\sqrt{2\pi}$ and

$$\frac{s}{\Omega} \to \frac{3}{2} (2\pi)^{1/8} \left(\frac{\Delta \Pi k_y^3 W}{\Omega^2} \right)^{1/4}.$$
 (36)

Unfortunately this limit does not directly apply. We are mainly interested in $k_y W/\mathcal{J} \gtrsim 0.01$, corresponding to $\alpha \lesssim 3.4$, i.e., at most order unity.

Our approximate Equation (32) corresponds to $f_{\rm US} \sim \alpha^3$, a good approximation for order unity α .

3.3. Incompressible Eigenfunctions

To visualize RWI modes, Figure 5 maps perturbed vorticity ζ_1 and velocity vectors v_1 for various growth rates and feature types. These incompressible eigenfunctions are similar to the standard global, compressible RWI (T. Ono et al. 2016). Corotation is near the vorticity minima marked with the dotted line.

The RWI mechanism is clearest for larger growth rates (bottom row). The pair of CRWs across corotation (analyzed in Section 3.1.1) is evident. This wave pair is shifted in the azimuthal phase, but radially symmetric for the bumps, and asymmetric for gaps and steps, consistent with their asymmetric potentials (Figure 1). The azimuthal phase shift causes flow through the vorticity minima to primarily enter regions of negative perturbed vorticity. This explanation of the growth mechanism is well known for general shear flows (E. Heifetz et al. 1999) and the RWI (T. Ono et al. 2016).

At lower growth rates (middle row), the phase shift decreases. The feeding of negative vorticity from the background into perturbations is less direct, entering narrow fingers near corotation. Even closer to marginal stability (top rows), the phase shift is nearly gone, and feeding via narrow glitches near corotation is harder to see.

For marginal stability, ζ_1 is nonzero and smooth through corotation. However, all growing modes have $\zeta_1 = 0$ at vorticity extrema (as shown by Equation (11)). This fact explains the necessity of small glitches near marginal stability and the width of prominent CRWs, which fit between a vorticity maximum and minimum (see Figure 1).

4. Compressible Results in the Shearing Sheet

We now analyze the CSS model of Sections 2.1 and 2.3.2. Compressible effects are captured by the value of k_yH (see below). Our incompressible results roughly correspond to the $k_yH \rightarrow \infty$ limit.

For an effective Mach number, we use the Keplerian shear across a length scale of $1/k_v$ to define

$$\mathcal{M}_{\text{eff}} \equiv \frac{\Omega/k_{y}}{c} = \frac{1}{k_{y}H}.$$
 (37)

RWI modes with $\mathcal{M}_{\rm eff} \lesssim 1$ behave incompressibly, which is expected of subsonic flows. In global protoplanetary disks, the RWI is moderately compressible for m=1 modes, and more incompressible for higher m (Section 6, point 3).

4.1. Compressible Stability Boundary

Figure 6 shows the effect of compressibility, measured by k_yH , on the RWI boundary. The bump feature is chosen and is representative, with quantitative shape effects noted below.

For $k_yH=1$, the stability boundary overlaps the incompressible limit $(k_yH\to\infty)$. As k_yH decreases, compressibility effects increase

For sufficiently small $k_y H \lesssim 0.01$, the stability boundary breaks into three distinct regions, approximately as

$$\frac{\Delta\Pi}{\Omega^2 W^2} \approx \begin{cases}
f_{\text{MS}} W \left(k_y + \frac{1}{4H} \right) & \text{if } W \lesssim H \\
0.4 j_{\text{MS}} & \text{if } H \lesssim W \lesssim k_y^{-1} \\
\infty & \text{if } k_y W \gtrsim g_{\text{MS}}.
\end{cases} (38)$$

The shape-dependent factors $f_{\rm MS}$, $g_{\rm MS}$ (Section 3.1) and $j_{\rm MS}$ (below) are order unity. For incompressible parameters, $k_y H \gtrsim 0.3$, this stability boundary reverts to the incompressible case, with no intermediate width region. For marginal compressibility, $k_y H \simeq 0.1$, these regions are not as distinct, with overlapping transitions.

For small widths, W < H, the compressible $(k_y H \ll 1)$ stability boundary follows $\Delta \Pi \approx f_{\rm MS} \Omega^2 W^3/(4H)$, independent of k_y . Compared to the incompressible $k_y W \ll 1$ boundary, $\Delta \Pi \propto W^3$ is identical, but compressible enthalpy features must be $\simeq 1/(4k_y H)$ larger for instability. This stabilizing effect generally arises from the fact that some of the energy is used to compress the flow (W. Blumen 1970).

Wide features and/or short wavelength modes, $k_y W \gtrsim g_{\rm MS} \sim 1$, are RWI stable, like the incompressible case. However, compressible modes are more unstable between $0.3 \lesssim k_y W \lesssim g_{\rm MS}$ (see Figure 6). This effect arises because Lindblad resonances, absent from the incompressible limit, approach the Rossby zone, as described below. Ultimately, the widest features require a global treatment (Section 5).

For intermediate widths, with $W \gtrsim H$ but $W \lesssim k_y^{-1}$, the stability boundary is approximately given by $\mathcal{J} = \Delta \Pi/(W^2\Omega^2) = 0.4j_{\rm MS}$, with $j_{\rm MS} \simeq 1$, 2.8, 3.0 for bumps, gaps, and steps, respectively. The value of $\min(\kappa^2) = 1 - \mathcal{J}/\mathcal{J}_\kappa \simeq 0.6$, 0.51, 0.54 for bumps, gaps, and steps, respectively, is more similar, emphasizing that κ^2 and being halfway to Rayleigh is more fundamental.

Figure 7 plots $\min(\kappa^2)/\Omega^2$ for marginal stability, moderate compressibility, $k_yH=0.03$, and different shapes. (The global models in this figure are discussed in Section 5.3.3.) For $W/H \gtrsim 2$, the stability boundary is halfway to Rayleigh with $\min(\kappa^2) \simeq 0.5 - 0.6\Omega^2$. For stronger stronger compressibility (smaller k_yH), $\min(\kappa^2)$ values would be more strictly constant (Figure 6).

In Figure 7, the $k_y W \sim 1$ stability boundary is off-scale at $W/H \sim 30$. For $W/H \lesssim 1$, the stability boundary approaches $\min(\kappa^2)/\Omega^2 = 1 - (f_{\rm MS}/\mathcal{J}_{\kappa})(W/H)/4$, following Equation (38).

While shape effects are minor in the shearing sheet, bumps most readily trigger RWI, at larger $\min(\kappa^2)$ values (Figure 7) and smaller enthalpy amplitudes (smaller $f_{\rm MS}$ and $j_{\rm MS}$ values, see Figure 3).

We next examine the origin of the three limits in Equation (38).

4.1.1. Small Width Compressible Boundary

In Section 3.1.1, incompressible instability for $k_y W \ll 1$ is given as the Y. Lithwick (2007) wave shearing time criteria $\Delta \zeta_0 t_{\rm sh} \gtrsim 1$. The corresponding $W \ll H$ compressible instability criterion is that the sound crossing time $t_{\rm sc} \equiv W/(\Omega H) \lesssim \Delta \zeta_0/\Omega^2$. Rotation

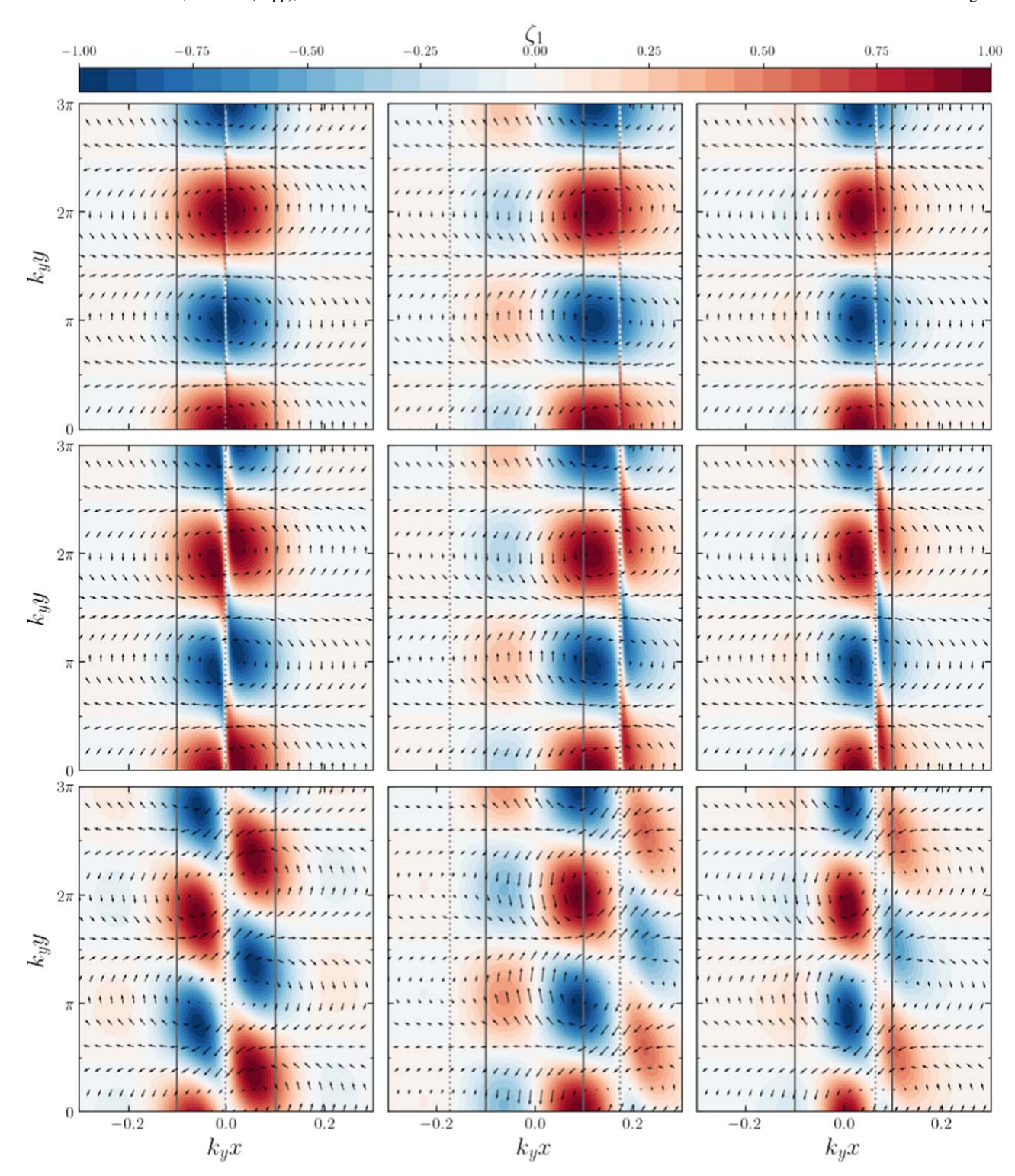


Figure 5. A map of perturbed vorticity, ζ_1 , for the RWI in the ISS, vs. x, y position, with arrows for the perturbed velocity v_1 . Rows from top to bottom have growth rates $s/\Omega \approx 10^{-3}$, 10^{-2} , and 10^{-1} , respectively. Columns from left to right consider enthalpy bumps, gaps, and steps, respectively. Solid vertical lines mark the feature width, $x = \pm W$. Dotted vertical lines locate the minima of the equilibrium vorticity, ζ_0 . The enthalpy amplitude \mathcal{J} was chosen to produce the desired growth, with wavenumber $k_y = 0.1/W$ in all cases.

appears explicitly in the compressible (but not the incompressible) instability condition, consistent with the discussion after Equation (12).

We can also adapt the WKB derivation of the $\mathcal{J}, k_y W \ll 1$ incompressible stability boundary in Section 3.1.1 to the compressible $k_y H \ll 1$, $W \lesssim H$ case. The main difference in this

case is that, from Equation (9b), the decay outside the Rossby zone follows $\Psi \propto \exp(-|x|/H)$. Thus, the slope change across corotation (now for Ψ) becomes $\Delta\Phi \sim -W/H$. In this limit, the potential depths are similar (to order unity), so the induced $\Delta\Phi \sim -\mathcal{J}$. Matching these two gives $\mathcal{J} \sim W/H$, the desired compressible boundary.

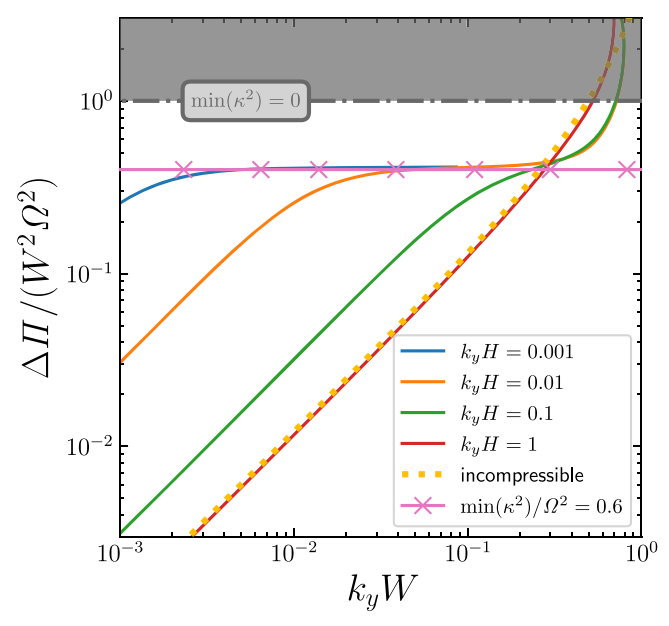


Figure 6. Marginal stability curves for the RWI of bumps in the CSS for different values of k_yH . The incompressible, $k_yH\to\infty$, limit (dotted yellow curve) and $\min(\kappa^2)=0.6$ references (pink line with x's) are shown. Axes and Rayleigh unstable region are as in Figure 3.

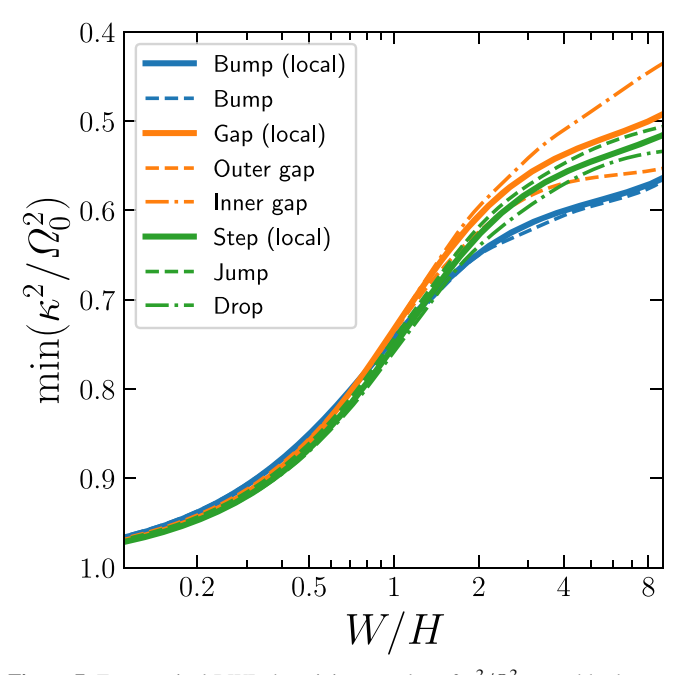


Figure 7. For marginal RWI, the minimum value of κ^2/Ω^2 caused by bumps, gaps, and steps (blue, orange, and green curves, respectively) vs. feature width. Solid curves show CSS models for $k_y H = 0.03$. Global models of bumps, outer gap edges and jumps (dashed curves) and of inner gap edges and drops (dotted–dashed curves) have $m=1,\ h=0.03$ (matching $mh=k_y H$). Global models break the symmetry between inner and outer gap edges and between jumps and drops.

4.1.2. Intermediate-width Stability Boundary

The halfway-to-Rayleigh instability criterion is given above as the scaled enthalpy condition, $\mathcal{J}\gtrsim 0.4j_{\rm MS}\sim 1$. In absolute terms, relative to $\Pi_{\rm b}\sim c^2$, this condition becomes $\Delta\Pi/c^2\gtrsim (W/H)^2$. Thus, widths larger than H require increasingly strong enthalpy features, a relevant point for the astrophysical origin of these features.

To explain this stability boundary, a negative potential at corotation $D(x_c) < 0$ gives a useful, necessary condition for instability (similar to Section 3.1.2). While simple to state, there are many terms in D to evaluate. These terms are stabilizing (or destabilizing) if they make a positive (or negative) contribution to $D(x_c)$.

We focus on the bump case with $x_{\rm c}=0$ for simplicity and take the $k_y W \ll 1$ and $\Delta \Pi \gg c^2$ (equivalent to $W \gg H$ as noted above) limits. These limits avoid the transitions to neighboring stability regimes.

The main stabilizing term is $\Sigma_0/(\mathcal{F}H_0^2)$, the usual source of the corotation barrier in disks. With $\Sigma_0/\mathcal{F} \propto \kappa^2$ this term is reduced near Rayleigh instability, and also, via H_0 , by disk heating. In our limits,

$$\frac{\Sigma_0}{\mathcal{F}H_0^2} \bigg|_{\mathbf{r}=0} \to \frac{3}{W^2} \bigg(\frac{1}{\mathcal{J}} - 1 \bigg). \tag{39}$$

The main destabilizing term is the corotation term $C_{\rm cor} = 2\Omega k_{\rm y} B/\Delta \omega$, though B'/2 also contributes. At corotation $B \propto d \ln(q_0)/dx$ diverges approaching Rayleigh instability.

Thus, a simple explanation of the halfway-to-Rayleigh result is that the stabilizing corotation barrier vanishes, and the destabilizing corotation resonance diverges for $\kappa^2 \to 0$. Thus, instability occurs somewhat before this point.

Our limits give

$$C_{\rm cor}(0) + \frac{B'(0)}{2} \to -\frac{3}{W^2} \left(\frac{3}{2(1-\mathcal{J})} + \frac{1}{3+\mathcal{J}} \right), \quad (40)$$

with the advertised $\mathcal{J} \rightarrow 1$ divergence.

Combining Equations (39) and (40), the necessary criterion D(0) < 0 becomes $\mathcal{J} > 0.29$. This condition is close to, but naturally below, the sufficient condition for bumps, $\mathcal{J} > 0.4$.

One insight from this analysis is that the equation of state effects should have a modest effect on this stability boundary, via H_0 and Σ'_0 . However, κ^2 is the dominant effect. We defer a more detailed study of thermodynamic, including baroclinic, effects.

4.1.3. Large-width Stability Boundary

The $k_y W \gtrsim 1$ condition for stability matches the incompressible case, which was physically justified in Section 3.1.1. We do generalize that argument to include compressibility, for reasons explored below.

The enhanced instability of compressible models for $0.3 \lesssim k_y W \lesssim 1$ is due to the proximity of Lindblad resonances, as noted above. While limited to a small region of parameter space, this result does go against the usual trend of compressibility hindering instability.

We expect nearby Lindblad resonances to enhance RWI because the outer wave propagation zones approach the corotation amplifier (R. Narayan et al. 1987; D. Tsang & D. Lai 2008). A similar effect is the reduction of the forbidden zone width, i.e., Toomre *Q* barriers, in self-gravitating disks (J. W. K. Mark 1976; P. Goldreich & S. Tremaine 1978).

We defer a detailed study of this effect, but note the basic properties of Lindblad resonances in our models. Their location, where $\Delta\omega^2=\kappa^2$, is at $|x|=\pm 2/(3k_y)$ in the limit of pure Keplerian flow in the shearing sheet (for corotation at x=0). This location clearly approaches $|x|\lesssim W$ for $k_yW\gtrsim 1$. Non-Keplerian flow affects the exact location of Lindblad resonances in the Rossby zone.

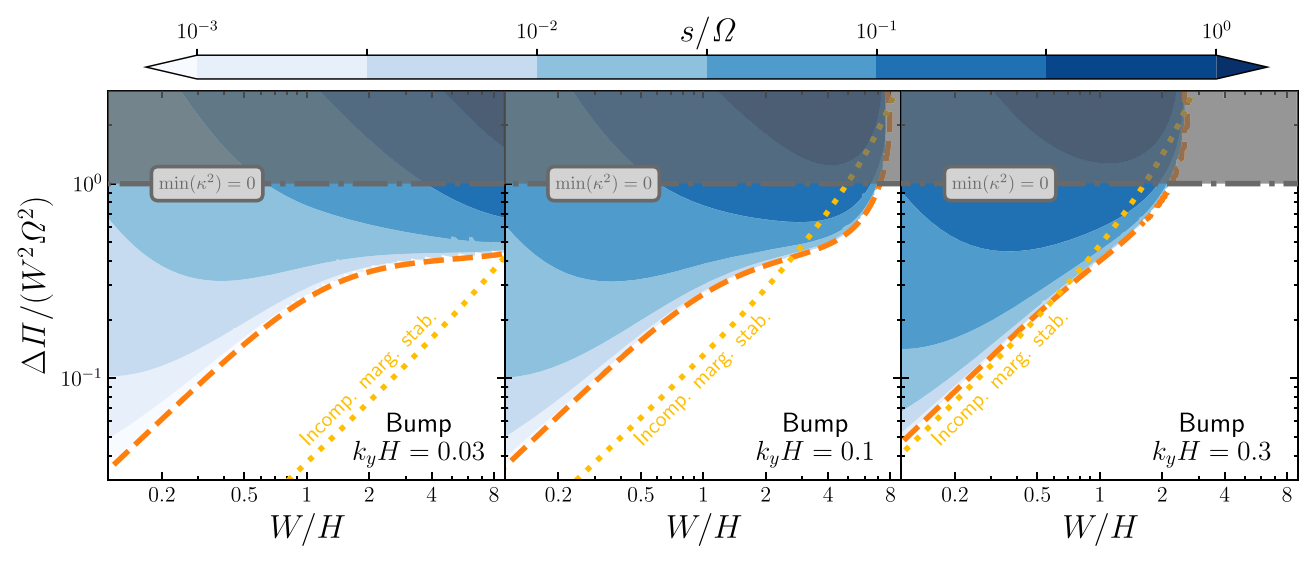


Figure 8. RWI growth rate, s, for bumps in the CSS, mapped vs. scaled bump amplitude, $\Delta\Pi$, and bump width relative to disk scale height, W/H. Different values of k_sH are shown from left to right. Compressible (dashed orange) and incompressible (yellow dotted) marginal stability curves are compared.

To understand why Lindblad resonances only affect compressible modes, note that density waves only propagate where D < 0. For Keplerian flow, this propagation region follows from the first two terms in Equation (9b) as $|x| > (2/3)\sqrt{1/k_y^2 + H^2}$, i.e., always with |x| > 2H/3 (P. Artymowicz 1993). This effective Lindblad resonance location is far from the Rossby zone for incompressible modes with $k_y H \gtrsim 1$.

The simplified analyses offered in other regimes are complicated by the presence of Lindblad singularities (where $\mathcal{F} \to \infty$) in the Rossby zone (see Figure 2). Lindblad singularities can be removed from the ODE (P. Goldreich et al. 1986). However, they are replaced by "sonic" singularities at $|x| \simeq 2H/3$, which also lie in the Rossby region in this W > H regime. We thus defer further analytic exploration of this regime.

4.2. Compressible Growth Rates

Figure 8 plots the growth rates for three different levels of compressibility, $k_yH=0.03$, 0.1, 0.3, from stronger to weaker, which also corresponds to a range of wavelengths from long to short. The bump case is shown, but other shapes are similar. The width is plotted as W/H, compared to k_yW in Figure 6 for a different perspective. The characteristic value of $k_yW=0.3$ (where compressible effects transition from stabilizing to destabilizing, as described above) lies at W/H=10, 3, 1, respectively, in these plots.

For fixed values of $W/H \lesssim 1$, the stability boundary is similar for the longer wavelength (more compressible) cases $k_yH = 0.03$, 0.1 but higher for $k_yH = 0.3$ (pushed by the incompressible limit). However, in the unstable region, larger k_yH modes grow faster.

For larger fixed values of $W/H \gtrsim 1$ models with smaller k_yH have an extended region of instability, out to $W/H \sim 1/(k_yH)$, but only have faster growth (than larger k_yH modes) close to the stability boundary.

More quantitatively, we showed that incompressible growth rates are approximately $s_{\rm inc} \sim (\Omega k_y^2 \Delta \Pi)^{1/3}$. For $k_y H \lesssim 0.1$, the compressible growth rates in Figure 8 are better characterized

by a reduced rate:

$$s_{\rm comp} \sim (\Omega k_{\nu}^3 H \Delta \Pi)^{1/3}$$
 (41)

for regions not too close to the stability boundary. As with the incompressible case, the growth rate has a weak dependence on feature width, W, and increases with k_y in the unstable region.

For quick estimates of RWI growth, Equation (38) can be used to determine if parameters are unstable, while the growth rate can be estimated as $\min(s_{\text{inc}}, s_{\text{comp}})$ for parameters a factor $\gtrsim 2$ from the stability boundary.

5. Comparison to Global Models

To understand the validity and limitations of our shearingsheet models, we compare them to global, cylindrical disk models. We demonstrate that shearing box models are valid for narrow features with sufficiently small W/R_c , and investigate the role of global disk parameters $m = k_v R_c$ and $h = H/R_c$.

We describe our global enthalpy features and compare them to other parameterizations in Section 5.1. We analyze the Rayleigh stability boundary in global models in Section 5.2. We compare the RWI in the shearing-sheet and global models in Section 5.3, and finally address RWI in dust traps in Section 5.4.

5.1. Global Disk Models

To best compare to our shearing-sheet models, our global models use an enthalpy feature of

$$\Pi_0(R) = \left(\frac{R}{R_c}\right)^q [\Pi_b + \Delta \Pi S(\Delta R/W)], \tag{42}$$

with $\Delta R = R - R_c$, power law q, and using the same shape functions S as Equation (13).

For the same polytropes, $P_0 \propto \Sigma_0^{\Gamma}$, Equation (18) generalizes to

$$\Sigma_0(R) = \Sigma_b \left(\frac{R}{R_c}\right)^n \left[1 + \frac{\Delta\Pi}{\Pi_b} S(\Delta R/W)\right]^{\frac{1}{\Gamma-1}},$$
 (43)

with $n = q/(\Gamma - 1)$. We again set $\Gamma = \gamma = 4/3$ and set n = q = 0 for simplicity in this work.

Works not using our enthalpy formulation can still be compared to our results. Surface density features (T. Ono et al. 2016; E. Chang et al. 2023),

$$\Sigma_{0,\Sigma}(R) = \Sigma_{b} \left(\frac{R}{R_{c}} \right)^{n} \left[1 + \frac{\Delta \Sigma}{\Sigma_{b}} S_{\Sigma}(\Delta R, W) \right]. \tag{44}$$

are equivalent to our enthalpy formulation, with $\Sigma_0 \simeq \Sigma_{0,\Sigma}$, for

$$\frac{\Delta\Sigma}{\Sigma_{b}} S_{\Sigma} \simeq \begin{cases}
\frac{1}{\Gamma - 1} \frac{\Delta\Pi}{\Pi_{b}} S & \text{if } \frac{\Delta\Pi}{\Pi_{b}} \ll 1, \\
\left(\frac{\Delta\Pi}{\Pi_{b}} S\right)^{\frac{1}{\Gamma - 1}} & \text{if } \frac{\Delta\Pi}{\Pi_{b}} \gg 1.
\end{cases} (45)$$

For small amplitudes the shapes are the same and the amplitudes are similar. Even the isothermal $\Gamma=1$ case follows from $(\Gamma-1)\Pi_b\to c^2/\gamma$ (Equation (19)). For larger amplitudes, neither amplitudes nor shapes are the same, so comparisons require more care.

Instead of the above analytic comparison, for general disk features, the corresponding enthalpy profile $\Pi_0(R)$ can be computed, and the amplitude and width measured. For barotropic models, the profile is simply $\Pi_0 = \int \!\! dP_0/\Sigma_0$. For nonbarotropic disks,

$$\Pi_0(R) = \Pi_0(R_{\rm r}) + \int_{R_{\rm r}}^{R} \frac{dP_0/dR'}{\Sigma_0} dR',$$
 (46)

for arbitrary values of the reference disk location, R_r , and $\Pi_0(R_r)$. The reference enthalpy is irrelevant, as a reference sound speed c (which is not arbitrary) can be used instead. Thus, with some effort, the enthalpy properties of any disk feature can be measured and applied to the results of this work.

5.2. Rayleigh Instability in Global Models

The results for our global models are shown in Figure 9 for bumps and Figure 10 for other shapes. In global models, the shearing-sheet symmetry of inner versus outer gap edges and jumps versus drops is broken. We show these additional cases.

We first discuss the location of the Rayleigh stability boundary. In shearing-sheet models, the Rayleigh stability boundary is at fixed \mathcal{J} (Equation (16), Figures 3, 6, and 8). For global models, the critical \mathcal{J} value changes for larger widths, W/R_c .

We describe Rayleigh instability as being "enhanced" (or "reduced") when the critical $\mathcal J$ value drops (or increases) for wider features. Of the shapes considered, most show enhanced Rayleigh instability to quite different degrees. Only the inner gap edge shows obviously reduced Rayleigh instability. The difference with the outer gap edge (which has the strongest enhancement) is striking. Curiously, the drop shape differs from the inner gap edge, which also can be considered a drop.

We wish to understand these effects since the Rayleigh stability boundary is crucial for our RWI analysis. We start with the orbital frequency

$$\Omega_0^2(R) = \Omega_K^2(R) + \frac{1}{R} \frac{d\Pi_0}{dR},$$
 (47)

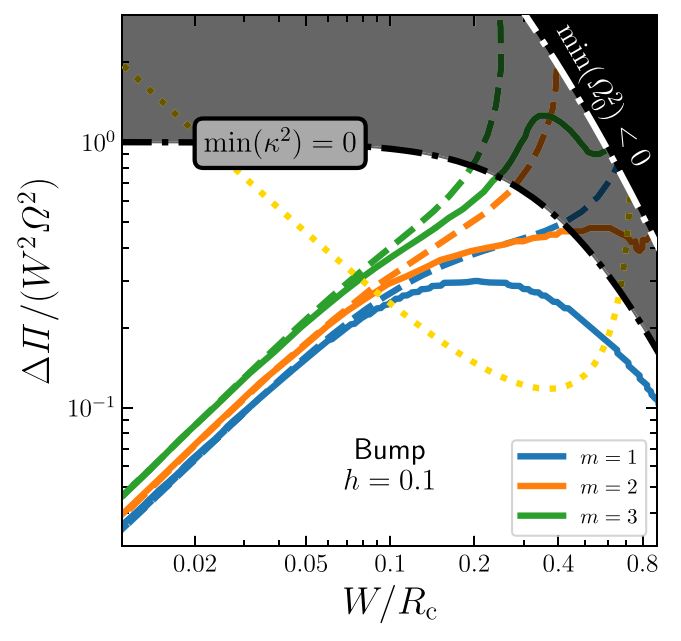


Figure 9. RWI marginal stability curves for bumps in an h = 0.1 global disk with azimuthal mode number m = 1, 2, 3 (solid blue, orange, and green curves, respectively). Dashed curves show shearing-sheet results for comparison. The grayed-out region is Rayleigh unstable. The dotted yellow curve gives the minimum amplitude of dust-trapping bumps.

where the Keplerian $\Omega_{\rm K}=\Omega_{\rm Kc}R_{\rm c}^{3/2}/R^{3/2}$. Using Equation (42) with q=0 and $\kappa^2=R^{-3}d(\Omega_0^2R^4)/dR$ gives

$$\frac{\kappa^2}{\Omega_{Kc}^2} = \left(\frac{R_c}{R}\right)^3 + \mathcal{J}\left[S''(X) + \frac{3W}{R}S'(X)\right] \tag{48}$$

for $X = \Delta R/W$, which reduces to the local limit, Equation (16), for W, $\Delta R \ll R_c$.

There are two main global effects in equation (48). The first "Keplerian" effect is the $(R_{\rm c}/R)^3$ term, which enhances Rayleigh instability if $R > R_{\rm c}$ at $\min(\kappa^2)$. For example, the outer edge of gaps and jumps have vorticity (and κ^2) minima at $R > R_{\rm c}$. Conversely, this effect reduces the Rayleigh stability for inner gap edges and drops.

The second "non-Keplerian" effect is given by the term 3(W/R)S'(X). Sub-Keplerian speeds (S'(X) < 0) contribute to lower vorticity and enhanced Rayleigh stability. This term is positive (negative) for jumps (drops) and outer (inner) gap edges. Thus, this second effect counteracts the first for these shapes (but not bumps, as discussed last).

Which effect dominates depends on shape details, especially how far the vorticity (and κ^2) minimum is from R_c . For a quantitative criterion, we Taylor expand Equation (48) about W=0, and evaluate at $R=R_{\rm m}=R_{\rm c}+X_{\rm m}$, the location of the local κ^2 minimum. This expansion shows that $\min(\kappa^2)$ is lower, and Rayleigh instability is enhanced if

$$f_W \equiv X_{\rm m} - \mathcal{J}S'(X_{\rm m}) = X_{\rm m} + \frac{S'(X_{\rm m})}{S''(X_{\rm m})} > 0.$$
 (49)

The final expression uses $\mathcal{J} = \mathcal{J}_{\kappa} = -1/S''(X_{\rm m})$, the small W Rayleigh stability boundary. Since $f_W > 0$ for outer gap edges (the Keplerian effect dominates) and for drops (the non-Keplerian effect dominates), the enhanced Rayleigh instability of these shapes is explained.

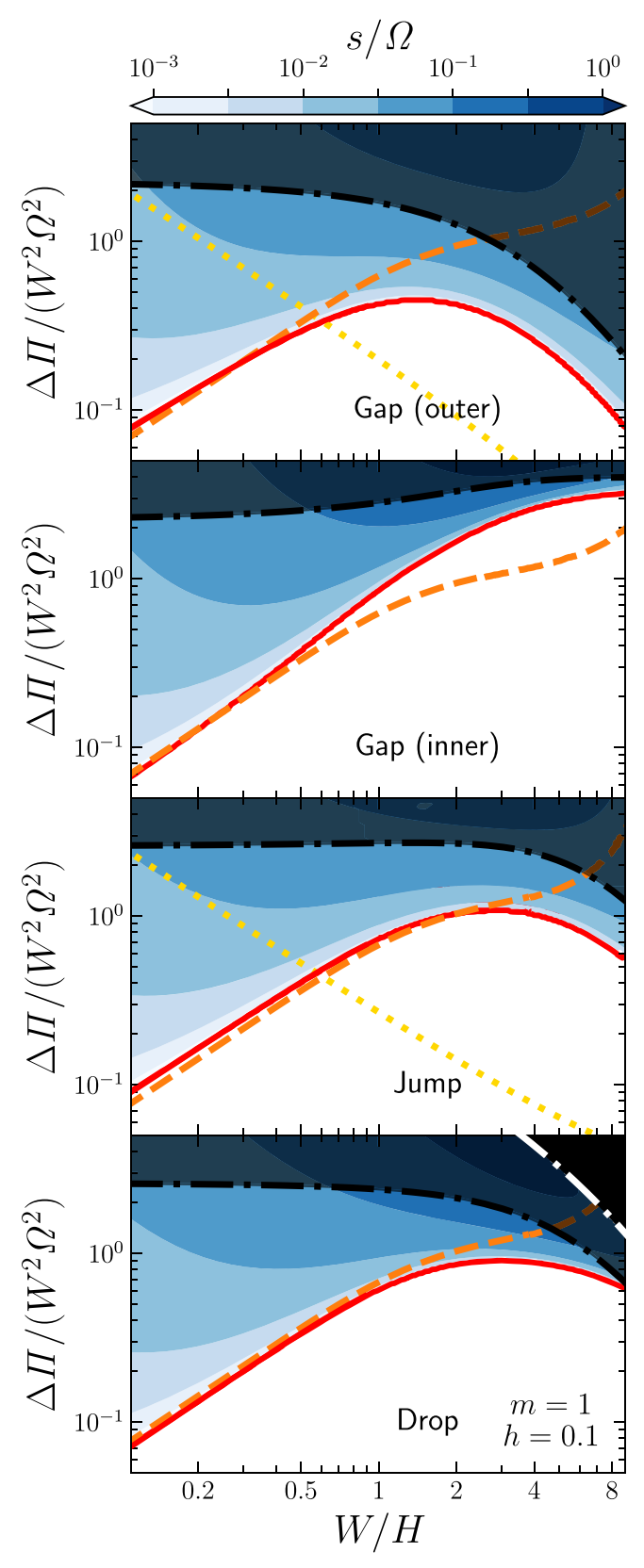


Figure 10. RWI growth rates of m=1 modes in our h=0.1 global disk for different shapes. Curves for marginal stability (solid), CSS marginal stability (dashed), Rayleigh marginal stability (black dotted–dashed), and marginal dust traps (dotted yellow) are shown.

Shapes with $f_W < 0$ (inner gap edges and jumps) are expected to show reduced Rayleigh instability. This expectation holds for inner gap edges, but jumps are more complicated. Rayleigh

stability is indeed reduced as $W \rightarrow 0$, but this small effect is not visible in Figure 10. At larger W/R_c , the first-order Taylor expansion is insufficient for jumps. As $X_{\rm m}$ increases for larger W/R_c , the Keplerian effect dominates, explaining the enhanced Rayleigh instability seen for jumps. The stronger competition between the two effects explains why the jump case shows a weaker enhancement, starting at larger W, compared to other shapes.

The bump case is special with $f_W = 0$, which is marginal by our simple criterion. However, since bumps have S'(X) < 0 for X > 0, both global effects combine constructively for the bump case, unlike the other cases. Thus, bumps have enhanced Rayleigh stability at larger W, with $\min(\kappa^2)$ shifting to X > 0.

From this analysis, we come to a better understanding of the Rayleigh stability boundary for wide disk features.

For even more extreme parameters than Rayleigh instability, outward pressure gradients can exceed stellar gravity, giving $\Omega_0^2 < 0$ (Equation (47)). The $\min(\Omega_0^2) = 0$ boundary appears in Figures 9 and 10. This boundary is shown to emphasize how extreme this region of parameter space is.

5.3. Global RWI versus Shearing Sheet

5.3.1. Effect of Mode Number m

Figure 9 plots the marginal stability curves for m = 1, 2, and 3 RWI modes in a h = 0.1 disk versus W/R_c for a bump shape (other shapes are addressed next). The equivalent CSS models have $k_yH = mh = 0.1, 0.2, 0.3$, and their stability curves are shown for comparison.

The shearing-sheet and global results agree very well for $W/R_{\rm c} \lesssim 0.1$, as expected. This agreement is excellent even for the most global m=1 modes. For $W/R_{\rm c} \gtrsim 0.1$, global and shearing-sheet results differ, more so for lower m. At larger widths, global bumps are more susceptible to the RWI than shearing-sheet bumps.

In Figure 9, the Rayleigh stability boundary deviates from constant \mathcal{J} , as described in Section 5.2. The m=1 mode curves to avoid the Rayleigh stability boundary, for $W/R_c \gtrsim 0.1$, another manifestation of the halfway-to-Rayleigh result.

The m = 2.3 modes do not share this behavior, crossing the Rayleigh boundary. Since these modes are only weakly compressible, with $mh = k_yH = 0.2$, 0.3, the halfway-to-Rayleigh behavior is not expected, and is also not seen in the comparison shearing-sheet models.

The shearing-sheet stability boundary at $k_y W \simeq 0.7$ is at $W/R_c \simeq 0.7/m \simeq 0.7$, 0.35, and 0.23 for the modes in Figure 9. The global models are more unstable, i.e., to larger widths than this boundary. This destabilizing effect diminishes for smaller W/R_c boundaries, as expected.

5.3.2. Effect of Feature Shape

Figure 10 plots marginal stability curves and growth rates for m=1, h=0.1 RWI modes for a range of shapes (but not bumps, shown in Figure 9). Global marginal stability is compared to shearing-sheet results for $k_yH=mh=0.1$. The agreement is again good for $W/R_c \lesssim 0.1$, i.e., $W/H \lesssim 1$ on this plot.

The inner and outer gap edges show the largest differences between global and shearing-sheet models, starting for $W/H \gtrsim 0.5$. The large distance between the gap center and vorticity minima ($\simeq 1.7W$, see Figure 1) is a natural explanation.

For most shapes, global models are more susceptible to the RWI than shearing-sheet models of equivalent parameters. Inner gap edges are the only exception (of the shapes considered). Inner gap edges are also the only shape to show reduced Rayleigh instability at larger widths (Section 5.2). The halfway-to-Rayleigh behavior of the RWI boundary thus also applies to global models as they deviate from the shearing-sheet approximation.

For narrow widths, $W/H \lesssim 1$, the growth rates in Figure 10 are consistent with the shearing sheet (see Figure 8 for $k_yH=0.1$), similar for all shapes, and given approximately by Equation (41). For wider features, we do not offer a global correction to this analytic approximation, as the effects seem shape dependent. The basic behavior is that growth rates steadily increase away from the RWI boundary.

5.3.3. Halfway to Rayleigh, Globally

We refer back to Figure 7 for the minimum value of κ^2/Ω_0^2 along the RWI boundary for global models with m=1, h=0.03 (a slightly thinner disk than above). The results are generally consistent with the equivalent $k_yH=mh=0.03$ shearing-sheet models. Note that global models compare to the orbital frequency $\Omega_0(R)$, not the fixed Ω of the shearing sheet.

For $W \gtrsim 2H$, all models have the RWI boundary occurring halfway to Rayleigh with $\min(\kappa^2/\Omega_0^2) \sim 0.5-0.6$. The inner and outer gap edges again show the largest global corrections at larger widths. Inner gap edges are again the most special case and the most resistant to RWI, especially for wide gaps. Inner gap edges require the lowest values of $\min(\kappa^2/\Omega_0^2)$ and the largest enthalpy amplitudes (Figure 10) to trigger RWI.

For thinner disks, $h \lesssim 0.01$, global corrections are less significant (for fixed W/H) and $\min(\kappa^2/\Omega_0^2)$ more constant along the RWI boundary. This effect is due to stronger compressibility, with $mh = k_y H < 0.01$ (Figure 6). Disks with moderate thickness, $0.03 \lesssim h \lesssim 0.3$, are more realistic but more complicated, due to intermediate compressibility and stronger global curvature effects.

While more study is needed, we expect the halfway-to-Rayleigh criterion to hold in cases more complex than our 2D, barotropic models. As noted in the introduction, E. Chang et al. (2023) were the first to identify the halfway to Rayleigh in several baroclinic models, which spanned the isothermal and constant surface density limits.

The precise location of the RWI stability boundary in 3D is not well studied. However, M.-K. Lin (2012) analyzed unstable RWI modes in 3D. A $W=0.05R_c=0.7H$ surface density feature in a locally isothermal disk has $\min(\kappa^2/\Omega_{\rm K}^2)=0.59$ and growth rates up to $s\simeq 0.06\Omega_0$ (for m=3).

A $W = 0.05R_c = 0.36H$ feature in a $\gamma = 5/3$ disk has $\min(\kappa^2/\Omega_K^2) = 0.47$ and growth rates up to $s \simeq 0.12\Omega_0$ (for m = 4). M.-K. Lin (2012) finds that these 3D growth rates are very similar to 2D rates, and these 3D results are also roughly consistent with our findings, despite model differences. In particular, the fact that these modes show significant growth is consistent with our Figure 7, which shows that W < H modes are more strongly unstable at halfway-to-Rayleigh conditions.

5.4. RWI in Dust Traps

E. Chang et al. (2023) examined which dust-trapping rings became unstable to—and would thus be modified by—the RWI. The condition for dust trapping is a maximum in the midplane pressure,

$$P_{\text{mid}} = \Omega_{\text{K}} \frac{P_0}{c_0} = \frac{\Omega_{\text{K}}}{\sqrt{\gamma}} \sqrt{P_0 \Sigma_0}, \qquad (50)$$

assuming a vertically isothermal structure.

Figures 9 and 10 show the minimum amplitude needed for dust trapping. Note that no dust traps exist for inner gap edges or drops since they reinforce $dP_{\rm mid}/dR < 0$ instead of reversing it. Dust traps that are stable to RWI lie in the parameter space above the yellow dotted dust-trapping curves and below the solid RWI boundaries.

As in E. Chang et al. (2023), who only considered bumps, stable (to RWI) dust traps exist above a minimum width and for a range of intermediate amplitudes. This parameter space is larger for outer gap edges and jumps versus bumps for reasons that can be explained by an analysis of $P_{\rm mid}$ similar to that of κ^2 in Section 5.2.

We defer a more detailed study of dust trap stability that further extends the work of E. Chang et al. (2023). We mainly note that such an analysis is facilitated by the insights into the RWI boundary established in this work.

6. Conclusions

We examine the linear RWI with a suite of simplified models to gain a basic understanding of the conditions for instability and unstable growth rates. The disk features that trigger the RWI are best characterized by their enthalpy amplitude, $\Delta\Pi$, and width W. When different combinations of temperature and density produce the same enthalpy profile, the equilibrium velocity and vorticity profiles are the same (Equations (3), (4)). We apply enthalpy features with various shapes (Section 2.3) to a suite of models in the ISS (Section 3), the CSS (Section 4), and global models (Section 5). Our main insights, explored in detail in the text, follow.

- 1. The RWI in the ISS is simply characterized by two dimensionless parameters: the scaled enthalpy amplitude $\mathcal{J} = \Delta \Pi/(\Omega W)^2$ and $k_y W$ (wavenumber times width). The ISS RWI can be understood analytically, including the stability boundary (Equations (27), (30)) and growth rate (Equations (32), (34)). The ISS RWI has a similar mechanism and eigenfunctions to the full disk RWI and to generic shear instabilities (Figure 5).
- 2. The RWI in the CSS requires the additional parameter, k_yH (wavenumber times scale height), an inverse Mach number. Modes with $k_yH > 1$ behave incompressibly. Smaller k_yH values show stronger compressibility effects (Figure 6).

- 3. The RWI is moderately compressible in typical protoplanetary disks with aspect ratios of $0.03 \lesssim h \lesssim 0.3$ (E. Chiang & A. N. Youdin 2010). Specifically, m = 1 azimuthal modes have $k_y H = mh \rightarrow h$, and are compressible, while $m \gtrsim 1/h$ modes are incompressible.
- 4. The RWI is usually most readily triggered by the longest wavelength, m = 1 modes (T. Ono et al. 2016; E. Chang et al. 2023; Section 5.3.1). However, in very thin disks, modes with different m but $mh = k_yH \lesssim 0.01$ will have nearly the same RWI boundary, due to strong compressibility (Equation (38)).
- 5. Only disk features with widths $W \lesssim 1/k_y$ can trigger the RWI (Figures 3, 6). In global models with a feature at radius R_c , this limit, $W/R_c \lesssim 1/m$, is relevant (i.e., smaller than the disk) for m > 1 (Figure 9 and Section 5.3.1). This limit is roughly derived in Section 3.1.1.
- 6. The RWI boundary often lies "halfway-to-Rayleigh instability" in that $\min(\kappa^2)$ drops to $\sim 0.5-0.6 \,\Omega^2$. This behavior occurs for widths $H \lesssim W \lesssim 1/k_y = R_{\rm c}/m$ (Figure 7), a range that expands for thinner disks. This boundary is roughly derived in Section 4.1.2. While approximate, this condition is significantly closer to the actual stability boundary than the necessary Lovelace criterion (T. Ono et al. 2016; E. Chang et al. 2023).
- 7. For narrow features, with $W \lesssim H$ the RWI boundary follows $\Delta \Pi \propto W^3$ (Equation (38)). This scaling agrees with the low amplitude behavior in T. Ono et al. (2016), see Equation (45). We explain the relevant factors that turn this previously known proportionality into an equality.
- 8. The stability boundary for the RWI of the localized disk feature (with $W \lesssim 0.2R_{\rm c}$) can be approximated by Equation (38). The enthalpy amplitude and width must be calculated (see Section 5.1). For wider disk features, the halfway-to-Rayleigh criterion is a good approximation for m=1 modes (Figures 9, 10).
- 9. Shape effects are generally minor when comparing the same enthalpy amplitude and width. However, bumps are the most susceptible to RWI. Wide gaps show the largest global corrections compared to shearing-sheet models. The inner edges of wide gaps are the least susceptible to RWI (Figures 7, 10).

This final point implies that wide, symmetric planetary gaps on the outer gap edge should generally support more vigorous RWI and vortex formation. Vortices at the outer edges of gaps could be more prominent in simulations and observations for other reasons as well, including larger area, longer orbital, and viscous timescales, numerical resolution, and more dust trapping (W. Fu et al. 2014; A. Lobo Gomes et al. 2015; M. Hammer et al. 2017; Z. Regály et al. 2017). Alternately, our results imply that over longer times, the RWI should make wide planetary gaps more asymmetric, with closer and steeper inner edges. The radial power law of the background disk also affects gap asymmetries (N. P. Cimerman & R. R. Rafikov 2023).

Our simplified models neglect many physical effects, notably baroclinicity, cooling, 3D motions, and self-gravity. Previous works have studied the RWI with these effects and shown their importance (Section 1). More studies that carefully map the stability boundary and growth rates with additional physics would be useful.

Acknowledgments

We thank Leonardo Krapp, Juan Garrido-Deutelmoser, Gordon Ogilvie, Roman Rafikov, Kaitlin Kratter, Wlad Lyra, Orkan Umurhan, and other participants in the University of Arizona Star and Planet formation Theory (sptheory) and Planet Formation in the Southwest (pfits+) group meetings for inspiring discussions and advice. We acknowledge support from the NASA Theoretical and Computational Astrophysical Networks (TCAN) via grant No. 80NSSC21K0497.

ORCID iDs

Eonho Chang https://orcid.org/0000-0003-4703-2053 Andrew N. Youdin https://orcid.org/0000-0002-3644-8726

References

Artymowicz, P. 1993, ApJ, 419, 166

```
Blumen, W. 1970, JFM, 40, 769
Chang, E., Youdin, A. N., & Krapp, L. 2023, ApJL, 946, L1
Chiang, E., & Youdin, A. N. 2010, AREPS, 38, 493
Cimerman, N. P., & Rafikov, R. R. 2023, MNRAS, 519, 208
Cui, C., Tripathi, A., Yu, C., Lin, M.-K., & Youdin, A. 2024, MNRAS,
   submitted (arXiv:2407.02103)
de Val-Borro, M., Artymowicz, P., D'Angelo, G., & Peplinski, A. 2007, A&A,
   471. 1043
Drazin, P. G., & Reid, W. H. 2004, Hydrodynamic Stability (Cambridge:
   Cambridge Univ. Press)
Drążkowska, J., & Dullemond, C. P. 2018, A&A, 614, A62
Fu, W., Li, H., Lubow, S., & Li, S. 2014, ApJL, 788, L41
Fung, J., & Ono, T. 2021, ApJ, 922, 13
Goldreich, P., Goodman, J., & Narayan, R. 1986, MNRAS, 221, 339
Goldreich, P., & Lynden-Bell, D. 1965, MNRAS, 130, 125
Goldreich, P., & Tremaine, S. 1978, ApJ, 222, 850
Hammer, M., Kratter, K. M., & Lin, M.-K. 2017, MNRAS, 466, 3533
Heifetz, E., Bishop, C. H., & Alpert, P. 1999, QJRMS, 125, 2835
Hu, X., Tan, J. C., Zhu, Z., et al. 2018, ApJ, 857, 20
Huang, S., & Yu, C. 2022, MNRAS, 514, 1733
Johansen, A., Youdin, A., & Klahr, H. 2009, ApJ, 697, 1269
Johnson, B. M., & Gammie, C. F. 2005, ApJ, 626, 978
Klahr, H., Baehr, H., & Melon Fuksman, J. D. 2023, arXiv:2305.08165
Kuznetsova, A., Bae, J., Hartmann, L., & Mac Low, M.-M. 2022, ApJ, 928, 92
Latter, H. N., & Papaloizou, J. 2017, MNRAS, 472, 1432
Lesur, G., Flock, M., Ercolano, B., et al. 2023, in ASP Conf. Ser. 534
   Protostars and Planets VII, ed. S. Inutsuka et al. (San Francisco, CA:
   ASP), 465
Li, H., Colgate, S. A., Wendroff, B., & Liska, R. 2001, ApJ, 551, 874
Li, H., Finn, J. M., Lovelace, R. V. E., & Colgate, S. A. 2000, ApJ, 533, 1023
Lin, M.-K. 2012, ApJ, 754, 21
Lin, M.-K. 2013, ApJ, 765, 84
Lin, M.-K., & Papaloizou, J. C. B. 2010, MNRAS, 405, 1473
Lin, M.-K., & Youdin, A. N. 2015, ApJ, 811, 17
Lithwick, Y. 2007, ApJ, 670, 789
Liu, H., & Bai, X.-N. 2023, MNRAS, 526, 80
Lobo Gomes, A., Klahr, H., Uribe, A. L., Pinilla, P., & Surville, C. 2015, ApJ,
Lovelace, R. V. E., Li, H., Colgate, S. A., & Nelson, A. F. 1999, ApJ, 513, 805
Lyra, W., Yang, C.-C., Simon, J. B., Umurhan, O. M., & Youdin, A. N. 2024,
   arXiv:2406.17934
Manasreh, M. O. 2012, Introduction to Nanomaterials and Devices (1st ed.;
   Hoboken, NJ: Wiley)
Manger, N., Klahr, H., Kley, W., & Flock, M. 2020, MNRAS, 499, 1841
Mark, J. W. K. 1976, ApJ, 205, 363
Meheut, H., Yu, C., & Lai, D. 2012, MNRAS, 422, 2399
Narayan, R., Goldreich, P., & Goodman, J. 1987, MNRAS, 228, 1
Nelson, R. P., Gressel, O., & Umurhan, O. M. 2013, MNRAS, 435, 2610
Ono, T., Muto, T., Takeuchi, T., & Nomura, H. 2016, ApJ, 823, 84
Pinilla, P., & Youdin, A. 2017, in Formation, Evolution, and Dynamics of
   Young Solar Systems, ed. M. Pessah & O. Gressel (Cham: Springer), 91
Regály, Z., Juhász, A., & Nehéz, D. 2017, ApJ, 851, 89
Tsang, D., & Lai, D. 2008, MNRAS, 387, 446
Umurhan, O. M., Shariff, K., & Cuzzi, J. N. 2016, ApJ, 830, 95
Vanon, R., & Ogilvie, G. I. 2016, MNRAS, 463, 3725
```